

Research Article

Magnetron Sputtering a New Fabrication Method of Iron Based Biodegradable Implant Materials

Till Jurgeleit, Eckhard Quandt, and Christiane Zamponi

Chair for Inorganic Functional Materials, Institute for Materials Science, Faculty of Engineering, University of Kiel, Kaiserstrasse 2, 24143 Kiel, Germany

Correspondence should be addressed to Till Jurgeleit; tiju@tf.uni-kiel.de

Received 17 September 2015; Revised 3 December 2015; Accepted 6 December 2015

Academic Editor: Jörg M. K. Wiezorek

Copyright © 2015 Till Jurgeleit et al. This is an open access article distributed under the Creative Commons Attribution License, which permits unrestricted use, distribution, and reproduction in any medium, provided the original work is properly cited.

It was shown in the previous decade that pure-iron has a large potential as a biodegradable medical implant material. It is necessary to tailor the material properties according to the intended use of the device. It is of great interest to investigate not only the influence of processing on the material properties but also alternative fabrication methods. In this work for the first time magnetron sputtering in combination with UV lithography was used to fabricate free standing, patterned pure-iron thick films. For the intended use as biodegradable implant material free standing thick films were characterized in terms of microstructure, degradation performance, and mechanical properties before and after various heat treatments. The influence of microstructural changes on the degradation behavior was determined by linear polarization measurements. The mechanical properties were characterized by tensile tests. Microstructure, surface, and composition were investigated by scanning transmission electron microscopy (STEM), energy dispersive X-ray spectroscopy (EDX), and X-ray diffraction (XRD) measurements. The foils exhibited a preferential orientation in $\langle 110 \rangle$ direction and a fine grained structure. Furthermore they showed a higher strength compared to cast iron and corrosion rates in the range of 0.1 mm/year. Their mechanical properties were tuned by grain coarsening resulting in a slight increase of the degradation rate.

1. Introduction

The usage of metallic materials as medical implants such as stents, meshes, nails, plates, and screws nowadays is a common treatment. Implants often serve their purpose only during a healing period of 3–12 months [1, 2]; afterwards the presence of the implants involves the danger of complications such as stent restenosis and chronic inflammation reactions [3]. The best way to prevent such complications is the usage of degradable implants; therefore metal based, biodegradable materials are subject to intense research in recent years [1, 3–6]. The most prominent examples of biodegradable metals are magnesium and iron as well as some of their alloys [3]. Both metals are essential elements in the human metabolism. The degradation of pure-magnesium was reported to occur fast and with a significant amount of hydrogen evolution [7–10] while pure-iron degrades rather slow and without hydrogen evolution. Iron additionally exhibits a higher mechanical

strength compared to pure-magnesium [1, 10, 11]. In vivo studies by Peuster et al. [1, 12] with New Zealand rabbits and mini pigs showed that it is possible to implant degradable pure-iron stents in the descending aorta. No significant obstructions of the vessel caused by inflammation, neointimal proliferation, or thrombotic events were observed in the study. Neither local or systemic toxicity nor an enrichment of corrosion products in the organs was found; however they found the corrosion rate of pure-iron to be too slow.

In the previous decade several attempts were presented [4, 11, 13–22] with the aim to tailor the degradation performance and the mechanical properties of iron by influencing the grain structure or changing the material composition. In this work a new method to produce patterned and free standing pure-iron foils by magnetron sputtering in combination with UV-lithography is presented. The method is most commonly used in the thin film technology. The fabrication of bulk, free standing NiTi thin films via sputtering was demonstrated

by Zamponi et al. [23, 24]. Lima de Miranda et al. [25, 26] showed that by using 3D lithography or micro laser welding 3D structures like tubular stents can also be produced by magnetron sputtering. A similar method for the fabrication of biodegradable, free standing, structured Mg-alloy foils by magnetron sputtering was presented by Schlüter et al. [27–29]. In order to modify corrosion behavior and mechanical properties, the sputter technology offers not only the opportunity of depositing pure-iron and alloys but also the fabrication of iron multilayer composites with noncompound forming elements [30].

Depending on the application sputtering allows a very precise control of the layer thickness from submicron scale up to 100 μm or even more, by varying the process parameters. Another important feature for the fabrication of implants is the freedom of design which is possible by the lithographic patterning and allows resolutions in the μm range.

For the intended use as biodegradable implant material the free standing foils were characterized with respect to corrosion behavior, mechanical properties, and microstructure. Furthermore the influence of ex situ heat treatments on the material properties was investigated.

2. Materials and Methods

2.1. Specimen Fabrication and Preparation. All films were deposited using a vonArdenne CS730 cluster sputtering machine with a base pressure in the 10^{-8} mbar range.

In the first step a 0.5 μm thick Cu sacrificial layer was sputtered on a 4", 500 μm thick (100) oriented Si-wafer. The wafer was structured via UV-lithography followed by galvanic Cu-deposition in order to produce dog-bone shaped foils [18, 19]. Afterwards iron was deposited on these structured substrates. Due to the ferromagnetic nature of α -iron RF-sputtering was used to allow depositions at lower working gas pressures. A magnetically calibrated 8" disk made of 99.9% pure cast iron was used as target material. To determine the temperature during the deposition, temperature indicators were used. The sputter parameters are listed in Table 1.

After the deposition of the iron, selective wet etching of the sacrificial layer was performed, using a solution containing DI-water, NH_3 , and H_2O_2 in order to release the foils from the substrate. Finally the free standing, structured foils were cleaned in an ultrasonic bath with isopropanol and DI-water. In order to alter the microstructure the samples were annealed at 400°C, 600°C, and 800°C for two hours; additionally samples at 600°C were annealed for different times of 20 min, 1 h, and 2 h. The sputtered free standing Fe-foils (s-Fe) were annealed under reducing atmosphere (95% Ar and 5% H_2 VARIGON H5) in order to prevent oxidation.

2.2. Investigations of Microstructure. To determine the crystallinity and texture of the specimens XRD measurements were performed with a Seifert XRD-300 PTS X-ray diffractometer, employing monochromatic Cu- $\text{K}\alpha$ radiation. The θ - 2θ -absolute scans were performed in the range of 35° to 90° with 0.05° step width and 2 sec dwell time per step. Scanning transmission electron microscopy (STEM) was used to obtain

further information about the microstructures; serving this purpose cross sections of the foils were prepared by focused ion beam (FIB) using a Helios NanoLab 600 (FEI). STEM images were captured using bright field (BF) and high angular annular dark field (HAADF) detectors. The determination of the average grain size was done by evaluating SEM surface images with a line intersection method [31]. Scanning electron microscopy on an Ultra Plus device by Zeiss was used to investigate the surface and fracture areas of the samples.

2.3. Mechanical Properties. Tensile tests were performed for mechanical characterization. Therefore “dog-bone” shaped samples (Figure 1) with 0.5 mm strut width and 7 mm strut length were produced as explained previously. The thickness was homogenous for all samples and varied depending on the batch between 28 μm and 32 μm .

The uniaxial tensile tests were performed with a testing machine of the type BETA 5-5/6 \times 10 (Messphysik) using a special sample holder for thin samples. A straining rate of 0.4%/min was applied; the fracture criterion was set to 60% force reduction relative to the maximum applied force. For each heat treatment four samples were measured.

2.4. Corrosion Measurements. A VersaSTAT 3-300 potentiostat connected to a three-electrode cell was used for the electrochemical corrosion tests. Quadratic foils with an edge length of 15 mm and 10 μm thickness were used for the corrosion measurements. Since the foils exhibit mirror finish ($R_a = 14 \text{ nm} \pm 3 \text{ nm}$) after deposition no additional conditioning or polishing steps were required. The samples were mounted on a sample holder acting as the working electrode (WE) with an exposed area of 0.916 cm^2 . As counter electrode (CE) a Pt mesh as well as wire was used. An Ag/AgCl electrode in a 3-molar KCl solution acted as reference electrode (RE). Hank’s balanced salt solution (HBSS) (H1387 Sigma Aldrich), modified with sodium bicarbonate (0.35 g/L), was used as electrolyte. The temperature was held constant at 37°C. Furthermore a regulated CO_2 inlet was used to keep the pH value at 7.4 ± 0.05 . A schematic sketch of the setup is given in Figure 2.

After determining the corrosion potential U_c in an 4000 s long open circuit (OC) measurement, the measurement of the $I(U)$ curves was performed; for this the WE was polarized from -400 mV to $+400 \text{ mV}$ around U_c with a potential shift rate of 1 mV/s. The Tafel extrapolation method was employed to calculate the corrosion rate (CR) from the $I(U)$ curves [32, 33]. Using the exposed electrode area the current was converted into the current density. By fitting the linear regimes of the logarithmically plotted $j(U)$ curve followed by extrapolation to U_c , the corrosion current density j_c was determined. The corrosion rate was calculated using (1) which is based on Faraday’s law [32, 33]:

$$\text{CR} = \frac{j_c M}{n \rho F}. \quad (1)$$

Here M is the molar mass of the corroding species, ρ is the density, n is the number of transferred elementary charges per reaction step, and F is Faraday constant. Under the

TABLE I: Sputtering parameters.

Element	Power (W)	Pressure (mbar)	Ar gas flow (sccm)	Sputter rate (nm/s)
Cu	1000 (DC)	$2.3 \cdot 10^{-3}$	25	4.1
Fe	600 (RF)	$2.3 \cdot 10^{-3}$	35	0.6

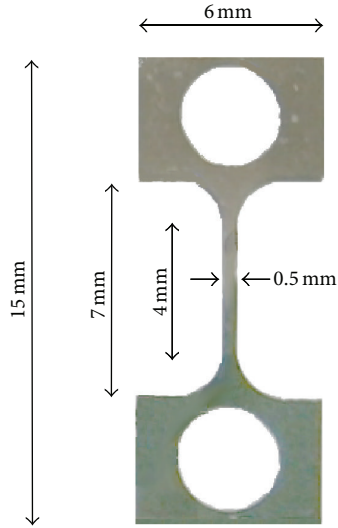


FIGURE 1: Dimensions of a “dog-bone” sample for tensile tests. The thickness of the different samples varied depending on batch between $28 \mu\text{m}$ and $32 \mu\text{m}$.

assumption based on studies by Zhu et al. [34] on the degradation kinetics of pure-iron in physiological fluids, iron is anodic dissolved as follows: $\text{Fe} - 2e^- \rightarrow \text{Fe}^{2+}$, so that $n = 2$. With $M = 0.056 \text{ kg/mol}$, $\rho = 7874 \text{ kg/m}^3$, and a conversion factor of 31536, the CR can be calculated in terms of mm/year. For each annealing temperature four samples were measured.

3. Results and Discussions

3.1. Characterization of Microstructure. The XRD measurements (Figure 3) and the STEM investigations (Figure 4) of the as-deposited s-Fe showed a fine grained structure with columnar growth and strongly preferred orientation in the $\langle 110 \rangle$ direction. Since the samples were measured on a Si-substrate, additionally the Cu (111) reflection from the sacrificial layer and Si (400) reflection from the substrate are visible. Only the α -Fe (110) reflection is present after all heat treatments independent of the temperature. The s-Fe shows no sign of film stress, since a relaxation of film stress during annealing would lead to a shift in the XRD peak position. The evaluation of the average grain size is shown in Figure 5. The obtained results are in good agreement with STEM images (Figure 4). A similar microstructure is observed for the as-deposited sample and those annealed at 400°C . After annealing at 600°C and two hours the samples show an inhomogeneous grain growth, whereas some grains grow up to diameters of $2.5 \mu\text{m}$; other grains retain the initial size ($0.5 \mu\text{m}$). After annealing for two hours at 800°C on the

one hand large grains up to $15 \mu\text{m}$ and on the other hand small grains in the range of $0.5 \mu\text{m}$ to $1 \mu\text{m}$ were observed.

Thornton and Hoffman [35–39] established the structure zone model which explains the dependence of the deposition conditions on the microstructure of sputtered films. The ratio of substrate temperature to melting temperature $T_{\text{sub}}/T_{\text{melt}}$ as well as the working gas pressure during the deposition has a strong influence on the film growth. Considering the measured substrate temperatures ($\approx 400^\circ\text{C}$), the ratio $T_{\text{sub}}/T_{\text{melt}} \approx 0.37$ results in small columnar defect rich grains (Figure 4, as-deposited). As expected annealing at 400°C shows no influence on the microstructure since the temperature is too low for a recrystallization ($T_{\text{sub}}/T_{\text{melt}} \approx 0.4$ – 0.5) or defect recovery. At 600°C ($T_{\text{sub}}/T_{\text{melt}} = 0.48$) the recrystallization starts. By increasing the annealing temperature to 800°C the recrystallization can propagate much faster, due to an enhanced generation of thermal vacancies and the increased self-diffusion. Since all samples before and after annealing show the columnar $\langle 110 \rangle$ oriented grains, a secondary recrystallization mechanism is assumed, where large grains grow at the expense of smaller ones by shifting their grain boundaries in order to minimize the grain boundary and dislocation energy. In a review paper by Thompson [40] dealing with the recrystallization in thin films, it is stated that recrystallization processes in nonbulk samples, where the smallest sample dimension is much larger compared to the grain size, surface, and interface energies play an important role. Particularly if the columnar grains extend over the entire sample thickness usually primary grain growth stops and secondary recrystallization processes occur. Thus the observed recrystallization behavior is explained by the grain structure and small sample dimensions of the sputtered iron foils.

3.2. Mechanical Properties. Some exemplary stress-strain curves of s-Fe after annealing with different annealing temperatures and annealing times are given in Figure 6. Mean values and standard deviation of the measured samples, as well as some literature values for biodegradable metals, are listed in Table 2. In general with increasing annealing temperature or time a decrease of strength and an increase of the ductility can be observed. The fracture area of an as-deposited tensile test sample is shown in Figure 7(a). A ductile fracture behavior with a clear necking can be observed. The samples annealed at 600°C and various times (Figure 6) show that the biggest change in the mechanical properties occurs between one- and two-hour heating time, giving an impression about the recrystallization speed. The obtained values are correlated to the annealing temperature and yield strength in Figure 7. According to the Thornton model [35–38] and the substrate temperature, the as-deposited structure is in the low temperature end of the transition zone where a large amount of defects

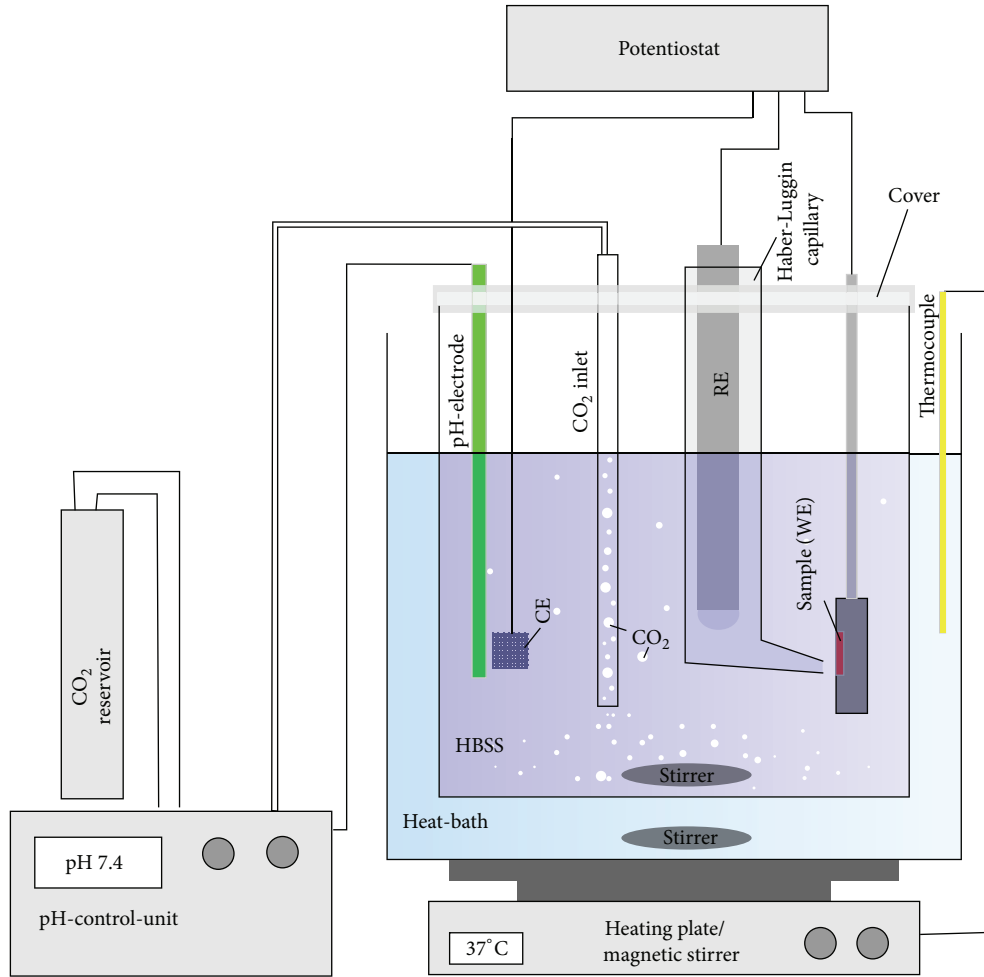


FIGURE 2: Schematic sketch of the corrosion measurement. A standard three-electrode setup is placed in the corrosion cell filled with Hank's buffered salt solution. The temperature is held at 37°C by a heating bath. By measuring the pH-value CO_2 inlet regulation the pH value of the solution is constantly kept at 7.4.

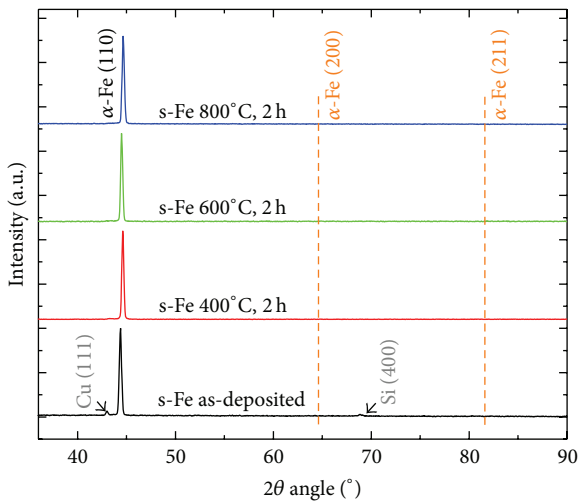


FIGURE 3: XRD θ - 2θ scan of as-deposited and annealed s-Fe foils. Due to the preferred (110) orientation before and after annealing, only the corresponding reflection is visible. No peak shift due to stress relaxation is noticeable. Also the possible α -Fe (200) reflection and α -Fe (211) reflection are indicated by vertical dash lines.

like dislocations, vacancies, and stacking faults is present. The reason for this is particles of high kinetic energy which hit the surface and thus enhance the formation of defects. Due to the substrate temperature during the deposition there is not enough activation energy for significant bulk diffusion which would lead to in situ annealing during the deposition. So the high initial strength is explained by the large amount of defects. Since the defects act as obstacles for dislocation movement and plastic deformation, respectively, the high defect density results in high internal stresses during the deformation which leads to an early fracture.

The presented results are in good agreement with studies on the mechanical properties of sputtered films reviewed by Bunshah [41]. In the review paper it was concluded that metals, sputtered in temperature regions corresponding to the transition zone, show a high strength and a low ductility comparable to those of mechanical worked material (see also Table 2, UD*-Fe). Due to the increased grain growth at high temperatures a decrease of the strength is observed. This behavior is explained by the grain coarsening in agreement with the well-known Hall-Petch relation [42].

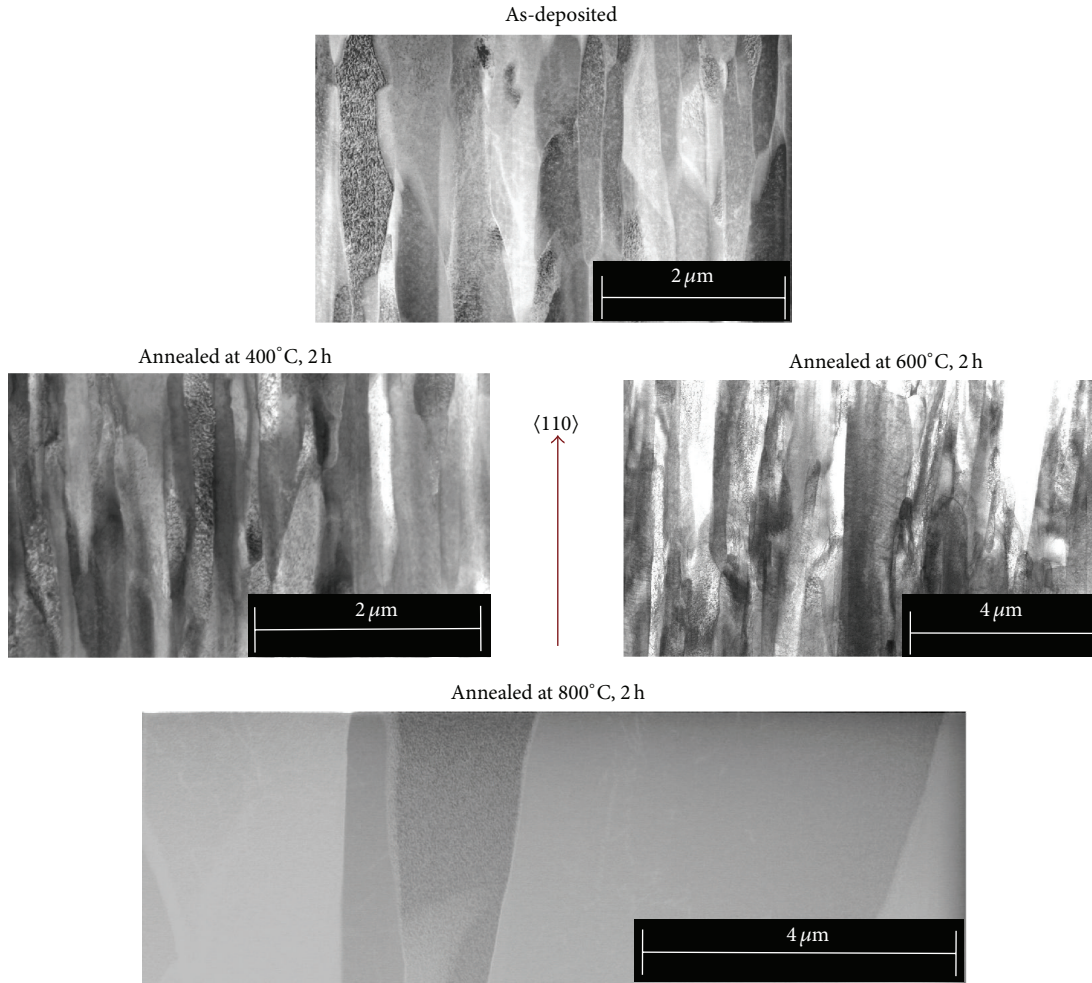


FIGURE 4: STEM images of s-Fe annealed at different temperatures for two hours.

TABLE 2: Measured mechanical properties of s-Fe after different annealing treatments and published literature values.

Sample	Yield strength (MPa)	Ultimate tensile strength (MPa)	Strain at fracture (%)
s-Fe as-deposited	606 ± 33	634 ± 33	1.4 ± 0.1
s-Fe annealed at 400°C, 2 h	604 ± 19	616 ± 9	1.6 ± 0.4
s-Fe annealed at 600°C, 20 min	612 ± 20	638 ± 10	1.3 ± 0.2
s-Fe annealed at 600°C, 1 h	568 ± 23	584 ± 33	2.0 ± 0.5
s-Fe annealed at 600°C, 2 h	381 ± 29	413 ± 9	13 ± 3.6
s-Fe annealed at 800°C, 2 h	267 ± 7	343 ± 4.7	20 ± 2.6
E [#] -Fe annealed at 550°C [14]	270 ± 6	292 ± 14	18.4 ± 4
E [#] -Fe annealed at 600°C [14]	130 ± 7	169 ± 9	32.3 ± 5
Cast iron annealed at 550°C [14]	140 ± 10	205 ± 6	$25.5 \pm \text{—}$
Fe35Mn [15]	234 ± 7	428 ± 7	32.0 ± 0.8
Armco Fe annealed [19]	$170 \pm \text{—}$	$270 \pm \text{—}$	$49.3 \pm \text{—}$
Fe(X) alloys as cast [18]	100–220	200–360	10–25
Fe(X) alloys as rolled [18]	360–450	430–850	5–9
UD* -Fe [20]	593 ± 2	600 ± 8	3.5 ± 2
UD* -Fe annealed [20]	246 ± 3	283 ± 5	34.8 ± 8
WE43 Mg alloy [8]	$198 \pm \text{—}$	$277 \pm \text{—}$	$17 \pm \text{—}$
316L SS [3]	$190 \pm \text{—}$	$490 \pm \text{—}$	$40 \pm \text{—}$

#Electroformed.

*Unidirectional rolled.

TABLE 3: Results of linear polarization corrosion measurements of s-Fe samples compared literature values.

Sample	Corrosion rate CR (mm/year)	Corrosion potential U_c (V)
s-Fe as-deposited	0.06 ± 0.02	-0.487 ± 0.052
s-Fe annealed at 400°C, 2 h	0.07 ± 0.01	-0.579 ± 0.015
s-Fe annealed at 600°C, 2 h	0.08 ± 0.04	-0.659 ± 0.016
s-Fe annealed at 800°C, 2 h	0.10 ± 0.01	-0.663 ± 0.081
E [#] -Fe as-deposited [14]	0.85 ± 0.05	-0.824 ± 0.018
E [#] -Fe annealed [14]	0.51 ± 0.06	-0.776 ± 0.020
Cast-iron annealed [14]	0.16 ± 0.04	-0.732 ± 0.016
Fe35Mn [15]	0.4 ± 0.1	N/A
Pure Fe [18]	$0.10 \pm \text{—}$	$-0.748 \pm \text{—}$
Fe(X) alloys as rolled [18]	0.10–0.18	$-0.680 \text{--} (-0.728)$
Armco Fe annealed [19]	0.21 ± 0.04	-0.735 ± 11
UD* -Fe annealed [20]	0.24 ± 0.02	-0.724 ± 4
Pure-Fe [10]	$0.10 \pm \text{—}$	$-0.748 \pm \text{—}$

[#]Electroformed.

*Unidirectional rolled.

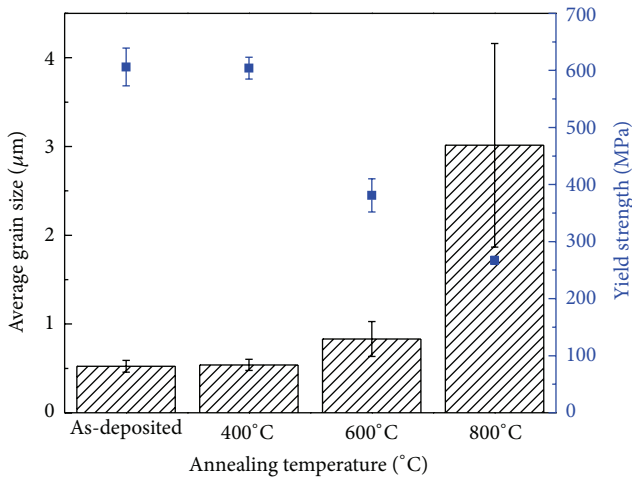


FIGURE 5: Graphical correlation between grain size, annealing temperature, and the yield strength of s-Fe annealed for two hours.

Due to the discussed recrystallization behavior the grain growth is nonhomogeneous; thus the very small grains which coexist with the larger ones act as obstacles for plastic deformation and therefore counteract the decrease of the strength explaining the comparably high residual strength after annealing. Increasing the annealing temperature and time strongly enhances the ductility of the material at the expense of its strength. This is mainly due to the recovery of defects which in turn reduces internal stresses necessary for dislocation movement. Due to patterning process the edges show a higher roughness compared to the surface (Figure 7(b)), which can act as a nucleus for crack initiation. Therefore the strain at fracture could be further increased by

improving the quality of the edges by chemical polishing or electropolishing, respectively.

A graphical summary of the results and comparison to literature values for biodegradable materials are given in Figure 8. Compared to the WE43 Mg alloy and pure-iron values from the literature [8, 14, 18–20] the presented annealed s-Fe shows a higher strength. The values are approaching those of the 316L SS alloy which acts as gold standard [3] for vascular stents and other iron based biodegradable Fe alloys [15, 18]. With regard to possible applications it has to be considered the best compromise between strength and ductility to tailor the mechanical properties by appropriate heat treatments.

3.3. Corrosion Measurements. Some exemplary linear polarization curves for s-Fe annealed at different temperatures are shown in Figure 9. With increasing grain size, a shift of the corrosion potential to more negative values can be observed. This is associated with a slight increase of the corrosion rate. The calculated mean values and standard deviations are summarized in Table 3. The results of this study are in good agreement with those found by Cheng and Liu [10, 18]. It is well known [13, 19–21, 43] that changes in the grain size affect the corrosion rate of iron. For biodegradable Mg-alloys it was shown [42, 43] that grain refinement leads to an improved corrosion resistance. Also Obayi et al. [19, 20] qualitatively observed the same behavior for pure-iron. Studies by Ralston et al. [44] and Nie et al. [21, 22] on the degradation kinetics of nanocrystalline (NC) and microcrystalline (MC) pure-iron concluded that, in metals which tend to the formation of passive oxide layers such as iron, an increase of the grain boundary density promotes the formation of a passivation layer. However

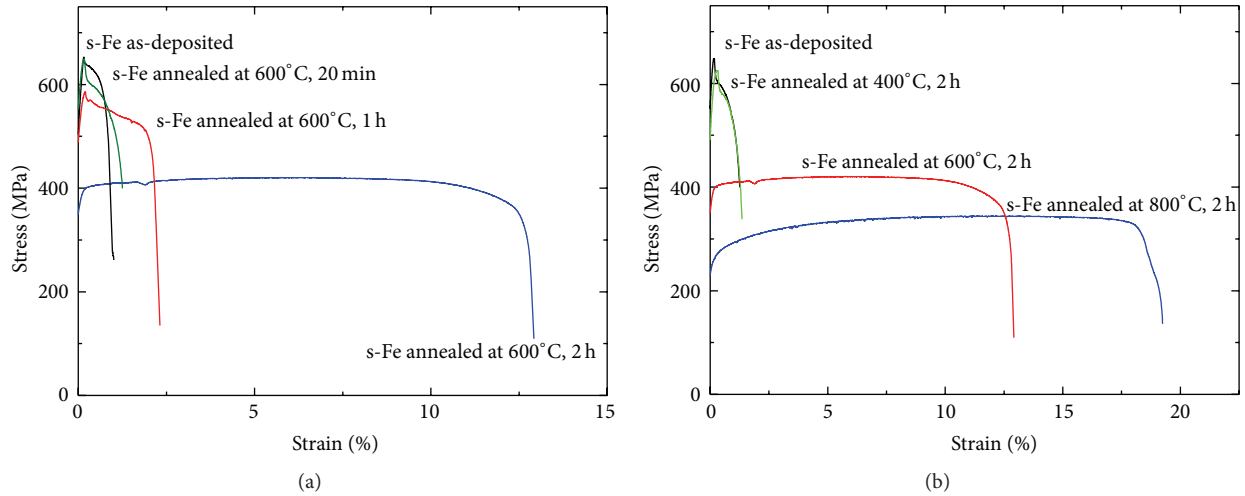


FIGURE 6: Exemplary stress strain curves of s-Fe annealed at 600°C for different dwell times (a) and at different temperatures for two hours (b).

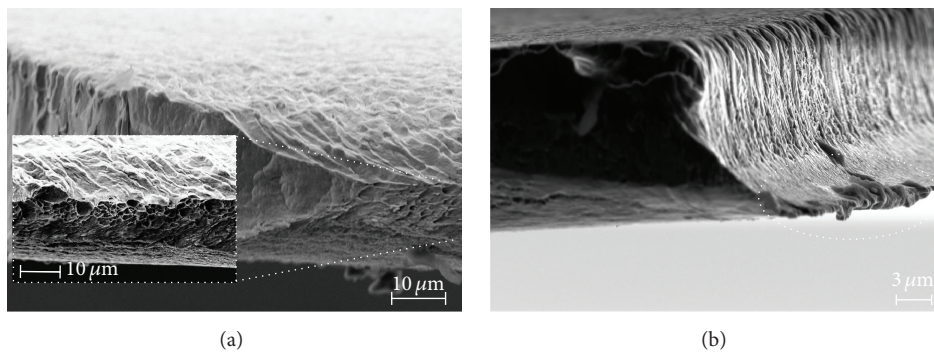


FIGURE 7: SEM image of fracture area (a), with significant necking. SEM image of the rough edge surface of an as-deposited dog-bone sample (b). The highlighted “feet” arises due to shadowing effects of the galvanic deposited Cu during sputtering on the substrate side.

studies by Moravej et al. [14] with electroformed iron (E-Fe) showed a decrease in the CR with increasing grain size; this behavior was related to the large amount of defects which are acting as active sites for corrosion. Since in general the sputtered microstructure shows similar characteristics, also a similar corrosion behavior could be expected. However the used target material in this study has a higher purity compared to those reported for the E-Fe. Therefore the high corrosion rates reported in the study could be related to the impurities acting as active sites for corrosion. The comparably low corrosion rate in this study can be explained by the high purity and fine-grained microstructure which promotes the formation of a passive layer. The slight increase of the corrosion rate with increasing grain size is assumed being attributed to a thinner and less stable passive oxide on larger grains [21, 22, 44]. However counteracting to this effect there is a decrease in the defect density which might be the reason for the rather weak influence of the grain coarsening on the corrosion rate.

4. Conclusion

It is shown that it is possible to produce free standing, patterned, pure-iron foils via magnetron sputtering. The foils show improved mechanical strength compared to cast Fe. It is possible to adjust the mechanical properties by a post-deposition annealing process. The samples show a comparable low degradation rate which is slightly increased by annealing and grain coarsening. Due to the higher mechanical strength thinner structures suffice to resist a load in a potential device, so that less material has to degrade. Moreover the presented method offers a large freedom of design which allows the fabrication of filigree structures. In combination with the high strength suitable designs can increase the surface to volume ratio and thus offer the potential to relativize the rather low corrosion rate.

Additionally there are a number of possibilities to accelerate the rate further by the deposition of more complex iron based systems. One possibility is the usage of prealloyed

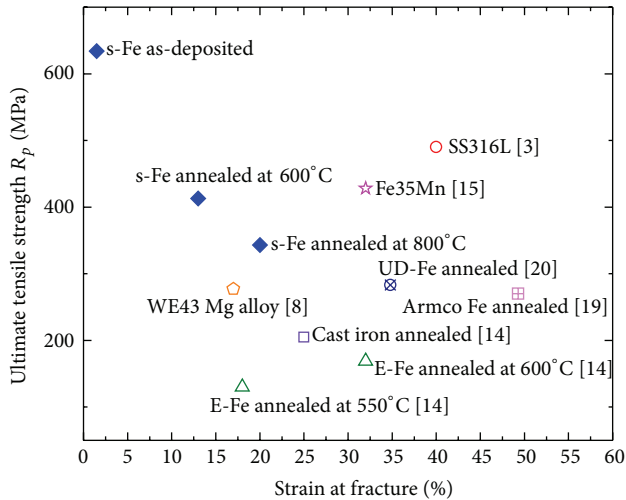


FIGURE 8: Overview of the mechanical properties found in this study for different annealed samples (as-deposited, 600°C, 2 h, and 800°C, 2 h) compared to literature values for biodegradable materials.

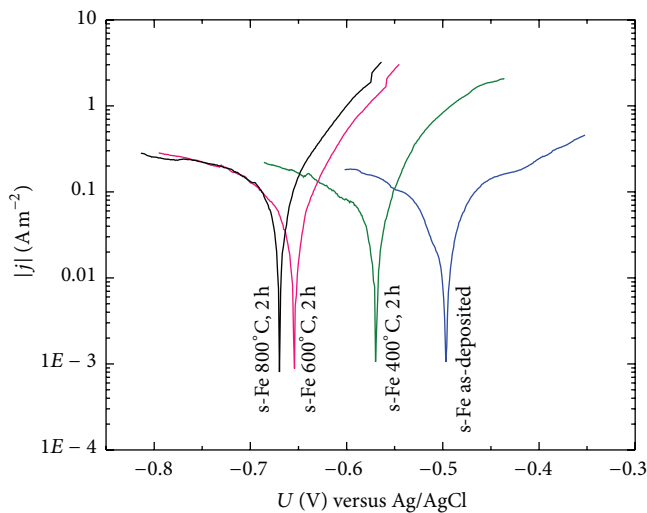


FIGURE 9: Exemplary Tafel-curves of s-Fe annealed at different temperatures for two hours. With increasing annealing temperatures a shift of U_c to more negative values and slight increase of j_c is observed.

sputter-targets with suitable elements. Another approach is the fabrication of multilayer composites with solvable or even nonsolvable elements. In combination with appropriate postdeposition heat treatments it is possible to fabricate in this manner tailored microstructures and material properties, respectively.

Investigation in terms of foil thickness and patterning resolution limits are subject of current research. Furthermore it has to be proven that the mentioned 3D lithography or microlaser welding [25, 26] can be applied for iron based sputtered material to allow the production of three dimensional devices like stents. Since the in vitro characterization can just compare different materials in terms of their

properties, in further studies in vitro cell tests have to be performed to assess how the material could behave in vivo.

The magnetron sputtering technique in combination with UV-lithography allows the fabrication of in situ patterned devices. Thus magnetron sputter technology offers a large potential to further improve the mechanical properties and corrosion behavior. Finally the presented method is a promising candidate in the fabrication technology of iron based, biodegradable devices with filigree designs.

Conflict of Interests

The authors declare that there is no conflict of interests regarding the publication of this paper.

Acknowledgments

Funding via DFG is gratefully acknowledged. The authors further acknowledge Jan Johansen and Bastian Hirsch for supporting this work in the tensile tests.

References

- [1] M. Peuster, C. Hesse, T. Schloo, C. Fink, P. Beerbaum, and C. von Schnakenburg, "Long-term biocompatibility of a corrodible peripheral iron stent in the porcine descending aorta," *Biomaterials*, vol. 27, no. 28, pp. 4955–4962, 2006.
- [2] P. K. Bowen, J. Drelich, and J. Goldman, "Zinc exhibits ideal physiological corrosion behavior for bioabsorbable stents," *Advanced Materials*, vol. 25, no. 18, pp. 2577–2582, 2013.
- [3] H. Hermawan, *Biodegradable Metals: From Concept to Applications*, Biodegradable Metals for Cardiovascular Applications, Springer, Heidelberg, Germany, 2012.
- [4] H. Hermawan, H. Alamdari, D. Mantovani, and D. Dubé, "Iron-manganese: new class of metallic degradable biomaterials prepared by powder metallurgy," *Powder Metallurgy*, vol. 51, no. 1, pp. 38–45, 2008.
- [5] A. Colombo and E. Karvouni, "Biodegradable stents: 'fulfilling the mission and stepping away,'" *Circulation*, vol. 102, no. 4, pp. 371–373, 2000.
- [6] E. Wintermantel and S. Ha, *Medizintechnik mit Biokompatiblen Werkstoffen und Verfahren*, Resorbierbare Implantate, Springer, Heidelberg, Germany, 2007.
- [7] M. P. Staiger, A. M. Pietak, J. Huadmai, and G. Dias, "Magnesium and its alloys as orthopedic biomaterials: a review," *Biomaterials*, vol. 27, no. 9, pp. 1728–1734, 2006.
- [8] F. Witte, N. Hort, C. Vogt et al., "Degradable biomaterials based on magnesium corrosion," *Current Opinion in Solid State and Materials Science*, vol. 12, no. 5-6, pp. 63–72, 2008.
- [9] F. Witte, "The history of biodegradable magnesium implants: a review," *Acta Biomaterialia*, vol. 6, no. 5, pp. 1680–1692, 2010.
- [10] J. Cheng, B. Liu, Y. H. Wu, and Y. F. Zheng, "Comparative in vitro study on pure metals (Fe, Mn, Mg, Zn and W) as biodegradable metals," *Journal of Materials Science & Technology*, vol. 29, no. 7, pp. 619–627, 2013.
- [11] Y. F. Zheng, X. N. Gu, and F. Witte, "Biodegradable metals," *Materials Science and Engineering R: Reports*, vol. 77, pp. 1–34, 2014.
- [12] M. Peuster, P. Wohlsein, M. Brüggemann et al., "A novel approach to temporary stenting: degradable cardiovascular

- stents produced from corrodible metal—results 6-18 months after implantation into New Zealand white rabbits,” *Heart*, vol. 86, no. 5, pp. 563–569, 2001.
- [13] K. D. Ralston and N. Birbilis, “Effect of grain size on corrosion: a review,” *Corrosion*, vol. 66, no. 7, 2010.
- [14] M. Moravej, F. Prima, M. Fiset, and D. Mantovani, “Electroformed iron as new biomaterial for degradable stents: development process and structure-properties relationship,” *Acta Biomaterialia*, vol. 6, no. 5, pp. 1726–1735, 2010.
- [15] H. Hermawan, D. Dubé, and D. Mantovani, “Degradable metallic biomaterials: design and development of Fe–Mn alloys for stents,” *Journal of Biomedical Materials Research Part A*, vol. 93, no. 1, pp. 1–11, 2010.
- [16] F. Witte, V. Kaese, H. Haferkamp et al., “In vivo corrosion of four magnesium alloys and the associated bone response,” *Biomaterials*, vol. 26, no. 17, pp. 3557–3563, 2005.
- [17] M. Schinhammer, P. Steiger, F. Moszner, J. F. Löffler, and P. J. Uggowitzer, “Degradation performance of biodegradable FeMnC(Pd) alloys,” *Materials Science and Engineering C*, vol. 33, no. 4, pp. 1882–1893, 2013.
- [18] B. Liu and Y. F. Zheng, “Effects of alloying elements (Mn, Co, Al, W, Sn, B, C and S) on biodegradability and in vitro biocompatibility of pure iron,” *Acta Biomaterialia*, vol. 7, no. 3, pp. 1407–1420, 2011.
- [19] C. S. Obayi, R. Tolouei, A. Mostavan et al., “Effect of grain sizes on mechanical properties and biodegradation behavior of pure iron for cardiovascular stent application,” *Biomatter*, 2014.
- [20] C. S. Obayi, R. Tolouei, C. Paternoster et al., “Influence of cross-rolling on the micro-texture and biodegradation of pure iron as biodegradable material for medical implants,” *Acta Biomaterialia*, vol. 17, pp. 68–77, 2015.
- [21] F. L. Nie, Y. F. Zheng, S. C. Wei, C. Hu, and G. Yang, “In vitro corrosion, cytotoxicity and hemocompatibility of bulk nanocrystalline pure iron,” *Biomedical Materials*, vol. 5, no. 6, Article ID 065015, 2010.
- [22] F. L. Nie and Y. F. Zheng, “Surface chemistry of bulk nanocrystalline pure iron and electrochemistry study in gas-flow physiological saline,” *Journal of Biomedical Materials Research Part B: Applied Biomaterials*, vol. 100, no. 5, pp. 1404–1410, 2012.
- [23] C. Zamponi, H. Rumpf, C. Schmutz, and E. Quandt, “Structuring of sputtered superelastic NiTi thin films by photolithography and etching,” *Materials Science and Engineering A*, vol. 481–482, pp. 623–625, 2008.
- [24] R. Lima de Miranda, C. Zamponi, and E. Quandt, “Micropatterned freestanding superelastic TiNi films,” *Advanced Engineering Materials*, vol. 15, no. 1-2, pp. 66–69, 2013.
- [25] R. Lima de Miranda, C. Zamponi, and E. Quandt, “Fabrication of TiNi thin film stents,” *Smart Materials and Structures*, vol. 18, no. 10, Article ID 104010, 2009.
- [26] G. Siekmeyer, A. Schüssler, R. Lima de Miranda, and E. Quandt, “Comparison of the fatigue performance of commercially produced nitinol samples versus sputter-deposited nitinol,” *Journal of Materials Engineering and Performance*, vol. 23, no. 7, pp. 2437–2445, 2014.
- [27] K. Schlüter, Z. Shi, C. Zamponi, F. Cao, E. Quandt, and A. Atrens, “Corrosion performance and mechanical properties of sputter-deposited MgY and MgGd alloys,” *Corrosion Science*, vol. 78, pp. 43–54, 2014.
- [28] K. Schlüter, C. Zamponi, N. Hort, K. U. Kainer, and E. Quandt, “Polycrystalline and amorphous MgZnCa thin films,” *Corrosion Science*, vol. 63, pp. 234–238, 2012.
- [29] K. Schlüter, C. Zamponi, A. Piorra, and E. Quandt, “Comparison of the corrosion behaviour of bulk and thin film magnesium alloys,” *Corrosion Science*, vol. 52, no. 12, pp. 3973–3977, 2010.
- [30] C. Zamponi, U. Schürmann, T. Jurgeleit, L. Kienle, and E. Quandt, “Microstructures of magnetron sputtered Fe Au thin films,” *International Journal of Materials Research*, vol. 106, no. 2, pp. 103–107, 2015.
- [31] ASTM E-112, “Metal test methods and analytical procedures,” in *Annual Book of ASTM Standards*, vol. 03.01, section 3, ASTM International, West Conshohocken, Pa, USA, 2007.
- [32] M. Stern and A. L. Geary, “Electrochemical polarization: I. a theoretical analysis of the shape of polarization curves,” *Journal of the Electrochemical Society*, vol. 104, no. 1, pp. 56–63, 1957.
- [33] D. A. Jones, “Electrochemical kinetics of corrosion: polarization methods to measure corrosion rate,” in *Principles and Prevention of Corrosion*, pp. 75–162, Pearson-Prentice Hall International, London, UK, 2005.
- [34] S. Zhu, N. Huang, L. Xu et al., “Biocompatibility of pure iron: in vitro assessment of degradation kinetics and cytotoxicity on endothelial cells,” *Materials Science and Engineering C*, vol. 29, no. 5, pp. 1589–1592, 2009.
- [35] J. A. Thornton and D. W. Hoffman, “Internal stresses in titanium, nickel, molybdenum, and tantalum films deposited by cylindrical magnetron sputtering,” *Journal of Vacuum Science & Technology*, vol. 14, no. 1, pp. 164–168, 1976.
- [36] J. A. Thornton, “Influence of apparatus geometry and deposition conditions on the structure and topography of thick sputtered coatings,” *Journal of Vacuum Science & Technology*, vol. 11, no. 4, pp. 666–670, 1974.
- [37] J. A. Thornton, “High rate thick film growth,” *Annual Review of Materials Science*, vol. 7, pp. 239–260, 1977.
- [38] J. A. Thornton, “The microstructure of sputter deposited coatings,” *Journal of Vacuum Science & Technology A*, vol. 4, no. 6, pp. 3059–3065, 1986.
- [39] J. A. Thornton and D. W. Hoffman, “Stress-related effects in thin films,” *Thin Solid Films*, vol. 171, no. 1, pp. 5–31, 1989.
- [40] C. V. Thompson, “Grain growth in thin films,” *Annual Review of Materials Science*, vol. 20, no. 1, pp. 245–268, 1990.
- [41] R. F. Bunshah, “3.1 mechanical properties of PVD films,” *Vacuum*, vol. 27, no. 4, pp. 353–362, 1977.
- [42] R. W. Cahn and P. Haasen, “Recovery and recrystallization,” in *Physical Metallurgy*, vol. 2, chapter 17, 4.2., p. 1589, Elsevier Science B.V., Amsterdam, The Netherlands, 4th edition, 1996.
- [43] L. Jinlong and L. Hongyun, “The effects of cold rolling temperature on corrosion resistance of pure iron,” *Applied Surface Science*, vol. 317, pp. 125–130, 2014.
- [44] K. D. Ralston, N. Birbilis, and C. H. J. Davies, “Revealing the relationship between grain size and corrosion rate of metals,” *Scripta Materialia*, vol. 63, no. 12, pp. 1201–1204, 2010.



Hindawi

Submit your manuscripts at
<http://www.hindawi.com>

